Fan, X., et al., 2021, Quaternary sodic and potassic intraplate volcanism in northeast China controlled by the underlying heterogeneous lithospheric structures: Geology, v. 49, https://doi.org/10.1130/G48932.1

SUPPLEMENTAL MATERIAL

Quaternary sodic and potassic intraplate volcanism in northeast China controlled by the underlying heterogeneous lithospheric structures

Xingli Fan[1,2], Qi-Fu Chen[1,4*], Yinshuang Ai[1,4*], Ling Chen[3,4], Mingming Jiang[1,4], Qingju Wu[5] and Zhen Guo[2]

[1]Key Laboratory of Earth and Planetary Physics, Institute of Geology and Geophysics, Chinese Academy of Sciences, Beijing 100029, China

[2]Department of Ocean Science and Engineering, Southern University of Science and Technology, Shenzhen 518055, China

[3]State Key Laboratory of Lithospheric Evolution, Institute of Geology and Geophysics, Chinese Academy of Sciences, Beijing 100029, China

[4]College of Earth and Planetary Sciences, University of Chinese Academy of Sciences, Beijing 100049, China

[5]Institute of Geophysics, China Earthquake Administration, Beijing 100081, China

INTRODUCTION

This supplemental material provides the detailed descriptions related to the seismic data (Table S1), seismic tomography methods (Figs. S1-S7 and Figs S9-S11), and resolution analyses including the traditional checkerboard test of phase velocity maps (Fig. S8) and synthetic restoring test of Vs models (Fig. S12). Seismic products generated in this study, consisting of the station-paired Rayleigh-wave phase velocity dispersion data used for the ambient noise tomography, intermediate 2-D Rayleigh-wave phase velocity models, and the final 3-D S-wave velocity model are all archived in the Seismic Array Laboratory, IGGCAS (doi:10.12129/IGGSL.Data.Observation, http://www.seislab.cn/), which can be downloaded via ftp://159.226.119.161/data/NECsaids/NE-China-Tomo-Data.

SEISMIC DATA

Seismic waveforms used in this study are collected from one permanent network and seven portable arrays, consisting of 145 permanent CEA stations (Zheng et al., 2010), 127 portable NECESSArray stations (Tao et al., 2014), 60 portable NECsaids stations (Wang et al., 2016), 40 portable NECsaids3 stations (Zhang et al., 2020), 42 portable WDLC stations (Lu et al., 2020), 20 portable DXAL stations (Peng et al., 2019), 6 portable XM stations (Zhang and Wu, 2019), and 6 portable NK stations (Ri et al., 2016). Detailed information about the number of stations and operating time range for each network is summarized below in Table S1.

Network name	***Number of stations***	***Operating time range***
CEA	145	2009.09-2018.06
NECESSArray	127	2009.09-2011.08
NECsaids	60	2010.07-2017.09
NECsaids3	40	2016.10-2018.10
WDLC	42	2015.06-2018.05
DXAL	20	2015.07-2017.06
XM	6	2015.07-2017.05
NK	6	2013.08-2015.10

Table S1. Detailed information about the seismic data used in this study.

AMBIENT NOISE TOMOGRAPHY

To extract fundamental mode Rayleigh-wave Empirical Green's Functions (EGFs) from the cross-correlations of ambient noise between pairs of stations, we adopt the data processing procedures previously described by Bensen et al. (2007) in detail. Here we briefly outline the major steps. For each station, vertical components of the raw continuous data are cut to daily segments and then decimated to 1 Hz. A band-pass filter of 2-100 s is applied to the resulting data after the corresponding instrument responses are removed. Running average time domain normalization and spectral whitening are employed to remove the effects of significant earthquakes, possible instrumental irregularities, and also broaden the bandwidth of the ambient noise. Daily ambient noise cross-correlations for each station pair are computed in the frequency domain and then stacked to obtain the final station-paired cross-correlation. Figure S1A shows an example of cross-correlation records between station MDJ (red triangle in Figure S1B) and all other stations. Clear Rayleigh-waves emerging in both the positive and negative lags with a nearly symmetric shape as shown in Figure S1A testify the high quality of our retrieved ambient noise cross-correlations.

In order to enhance the signal-to-noise ratio (SNR), positive and negative lags of the final station-paired cross-correlation are combined together to produce the so-called "symmetric component" (Bensen et al., 2007). Then, we perform the automatic frequency-time analysis (Levshin and Ritzwoller, 2001) to determine the phase velocity dispersion curves at the period band of 3-60 s. Phase velocity measurements with the SNR (as defined in Bensen et al. (2007)) smaller than 15 and the interstation spacing less than two wavelengths are discarded prior to further analysis. 2-D phase velocity maps are then generated utilizing a ray theory-based tomography method developed by Barmin et al. (2001). This tomographic method is based on minimizing a penalty function that depends on the smoothing damping parameter α, path density damping parameter β, and Gaussian smoothing parameter σ. During the inversion, these regularization parameters are chosen to optimize the agreement with the maps derived from the following earthquake tomography at overlapped periods. In this study, after a series of inversion tests, we set the values of α, β, and σ to be 600, 1, and 80. After conducting the trial inversion to obtain overly smoothed phase velocity maps, we compute the travel-time residual for each ray path and the outliers with travel-time residual larger than the two-standard-deviation value are rejected before the final inversion.

Figure S2A shows the number of ray paths as a function of period for the final inversion. The number of ray paths is larger than 10,000 throughout the period band and reaches the peak of around 65,000 at 15 s. The travel-time residual distribution at the period of 20 s, which centers near zero with a small standard deviation (STD less than 1 s) as shown in Figure S2B, statistically indicates that unrealistic measurements and significant outliers have been effectively removed. Phase velocity maps at selected periods (6 s, 10 s, 20 s, 30 s, 40 s and 50s) resulted from the ambient noise tomography are displayed in Figure S3. Additionally, six raw dispersion curves running through the CBS, JPH, ABG, HLH, NMH, and WDLC volcanoes are plotted in Figure S4. We can see that the phase velocities sampling the potassic volcanoes (NMH and WDLC) is systematically higher than the phase velocities sampling the sodic volcano (CBS, JPH, ABG and HLH), which is consistent with the 2-D phase velocity maps (Fig. S3) showing generally high-velocity anomalies around the potassic volcanoes and low-velocity anomalies surrounding the sodic volcanoes.

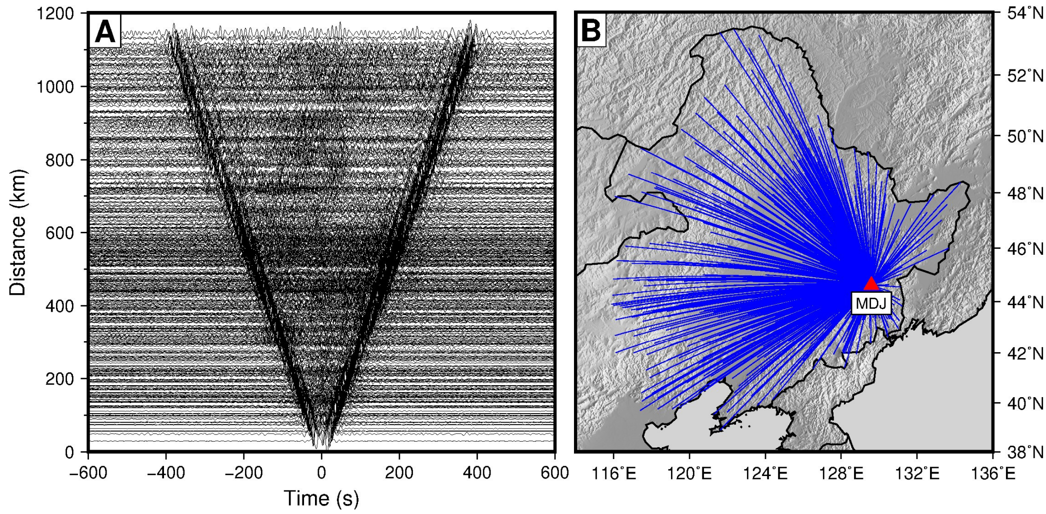

Figure S1. (A) An example of ambient noise cross-correlations between station MDJ (red triangle in B) and all other stations. (B) Corresponding inter-station ray paths between station MDJ and all other stations.

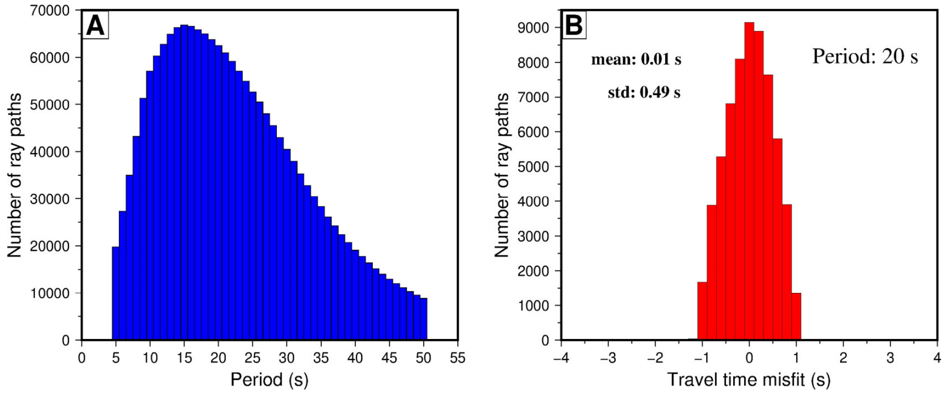

Figure S2. (A) Number of ray paths for the final inversion of ambient noise tomography as a function of period. (B) Travel-time residual histogram at the period of 20 s resulted from the final inversion of ambient noise tomography.

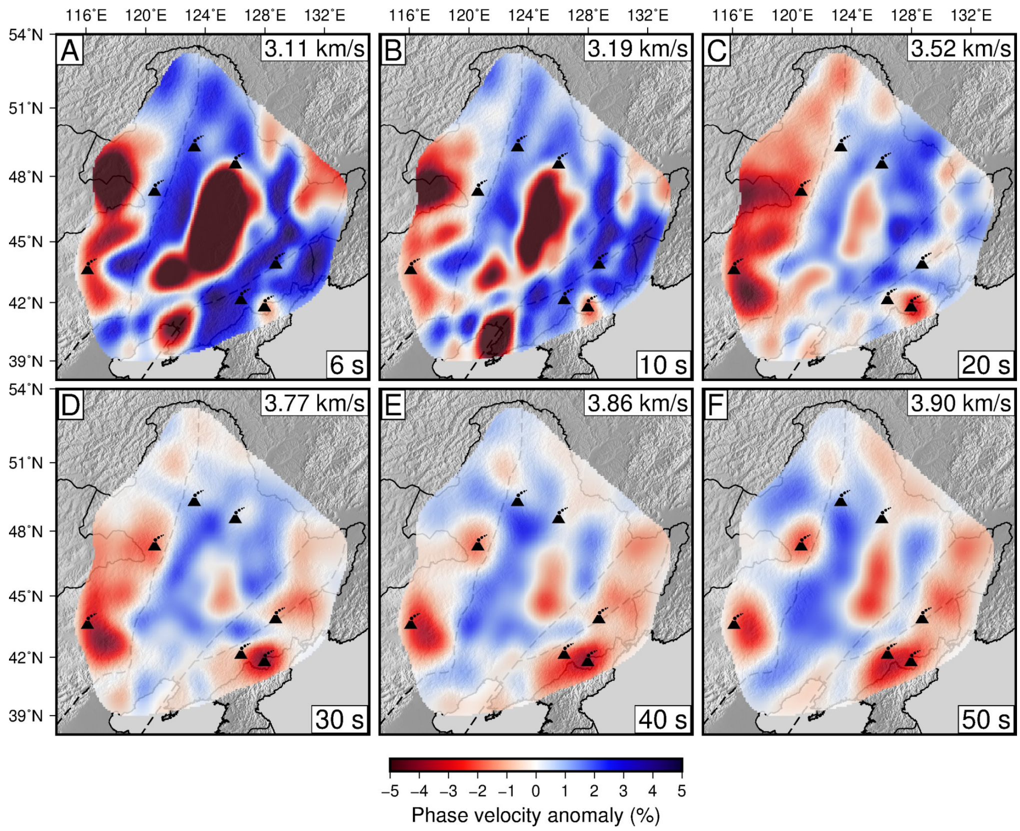

Figure S3. Phase velocity anomaly maps derived from the ambient noise tomography. The dashed lines are the North-South Gravity Lineament and Tanlu Fault as shown in Figure 1A. The black volcano symbols mark the Quaternary intraplate volcanoes with the distribution of their volcanic outcrops shown in Figure 1A. In each panel, the period and corresponding average phase velocity are labeled at the bottom-right and top-right corners, respectively.

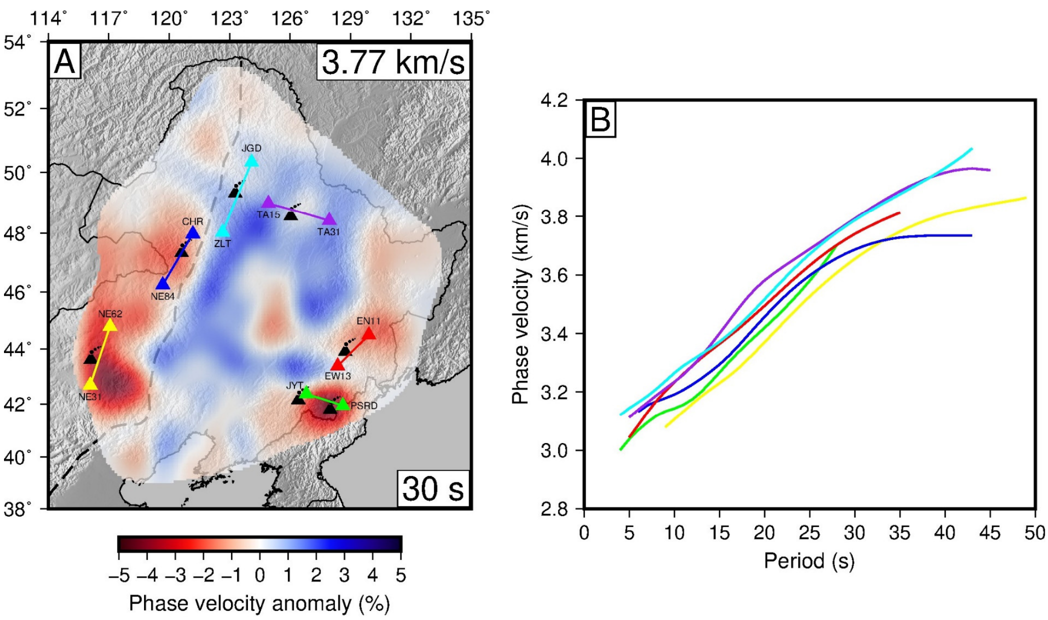

Figure S4. (A) shows the surface locations of the selected six station pairs (color coded lines) with their corresponding phase velocity dispersion curves plotted in (B). The background color image displayed in (A) is the phase velocity anomaly map at 30 s derived from the ambient noise tomography (Fig. S3D).

EARTHQUAKE TWO-PLANE WAVE TOMOGRAPHY

To extend the phase velocity range and therefore increase the resolvable depth of our Vs model, we perform the two-plane wave tomography (Forsyth and Li, 2005; Yang and Forsyth, 2006) to derive the fundamental mode Rayleigh-wave phase velocity maps at periods between 30 s and 143 s using teleseismic surface wave data. The two-plane wave tomography simulates the wavefield across the study region by the interference of two incoming plane waves (Yang and Forsyth, 2006). A 2-D finite frequency phase sensitivity kernel (Zhou et al., 2004) is employed to account for the sensitivities of surface waves to structural heterogeneities. The Gaussian length value used to smooth the 2-D sensitivity kernels, which has great effects on the model resolution and variance, is set as 80 km in this study to optimize the agreement with the maps derived from the previous ambient noise tomography at overlapped periods. A total of 629 earthquakes (Fig. S5A) with epicentral distance between 30° and 120°, magnitude greater than 6.0, and focal depth less than 50 km are collected to retrieve the fundamental mode Rayleigh-waves. Vertical seismograms with the SNR of teleseismic Rayleigh-wave signals less than 10 are discarded prior to further analysis. The selected earthquakes as shown in Figure S5A display a good azimuthal coverage in general with a slightly poor coverage to the east.

Since the assumption of two incoming plane waves would break down if the simulated single wavefield becomes too large (e.g., larger than 1,000 × 1,000 km^2 in this study), we divide our study region into four subregions and then model the incoming wavefield in each subregion using two plane waves. The whole study area is parameterized using a 2-D spatial grid with a node spacing of 0.5°. The inversion for 2-D phase velocity maps is invoked twice. First, we invert for the average phase velocity at each period and use it to calculate the updated 2-D sensitivity kernels. Second, we remove the outliers with phase travel-time misfit larger than 5 s from the surface wave dataset and then perform the inversion again to obtain the final 2-D phase velocity maps. The number of ray paths as a function of period retained after data selection is shown in Figure S5B. The number of remaining paths is larger than 4,000 at all periods and reaches the peak of around 20,000 at 45 s. Figure S6 exhibits the phase velocity maps at selected periods (30 s, 40 s, 60 s, 83 s, 111 s and 143 s) derived from the earthquake two-plane wave tomography.

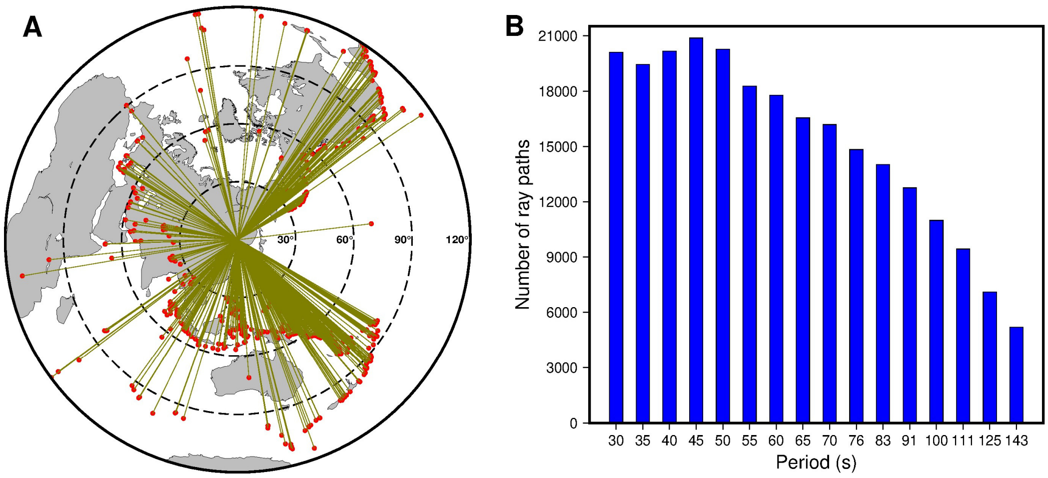

Figure S5. (A) Azimuthal distribution of teleseismic earthquakes (red dots) used in the two-plane wave tomography. (B) Number of ray paths for the two-plane wave tomography as a function of period.

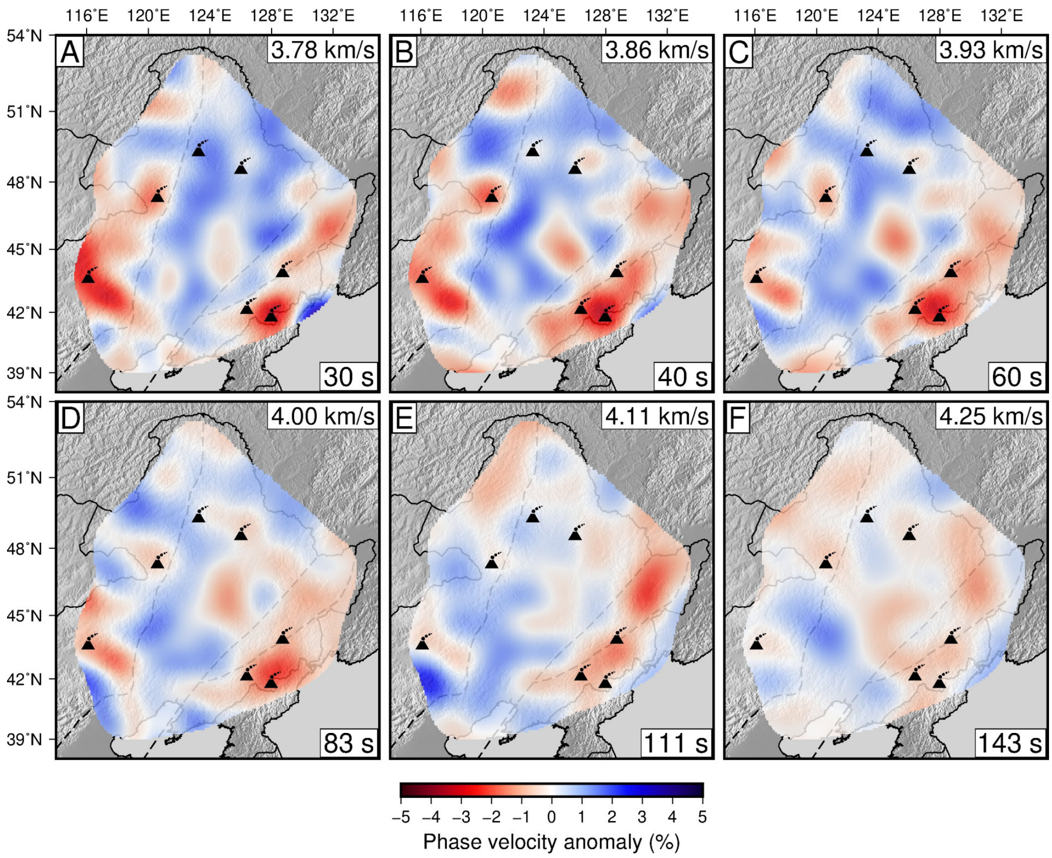

Figure S6. Phase velocity anomaly maps derived from the earthquake two-plane wave tomography. The dashed lines are the North-South Gravity Lineament and Tanlu Fault as shown in Figure 1A. The black volcano symbols mark the Quaternary intraplate volcanoes with the distribution of their volcanic outcrops shown in Figure 1A. In each panel, the period and corresponding average phase velocity are labeled at the bottom-right and top-right corners, respectively.

COMPARISON OF PHASE VELOCITY MAPS AT OVERLAPPED PERIODS

We compare the phase velocity maps derived from the ambient noise and earthquake two-plane wave tomography, and find they are quite consistent with each other. Figure S7 displays the comparison of phase velocity and corresponding uncertainty between the two different methods at the overlapped period of 40 s. The mean difference and the standard deviation of the phase velocity difference between the two maps are 3.4 m/s and 27.5 m/s, respectively (Fig. S7F). The uncertainty for the ambient noise tomography (Fig. S7C) increases considerably towards the periphery of the study region due to reduced crossing ray coverage, whereas the uncertainty for the earthquake two-plane wave tomography (Fig. S7D) is generally evenly distributed throughout the study region since the used earthquakes that generate the incoming rays are located outside the study region from all directions.

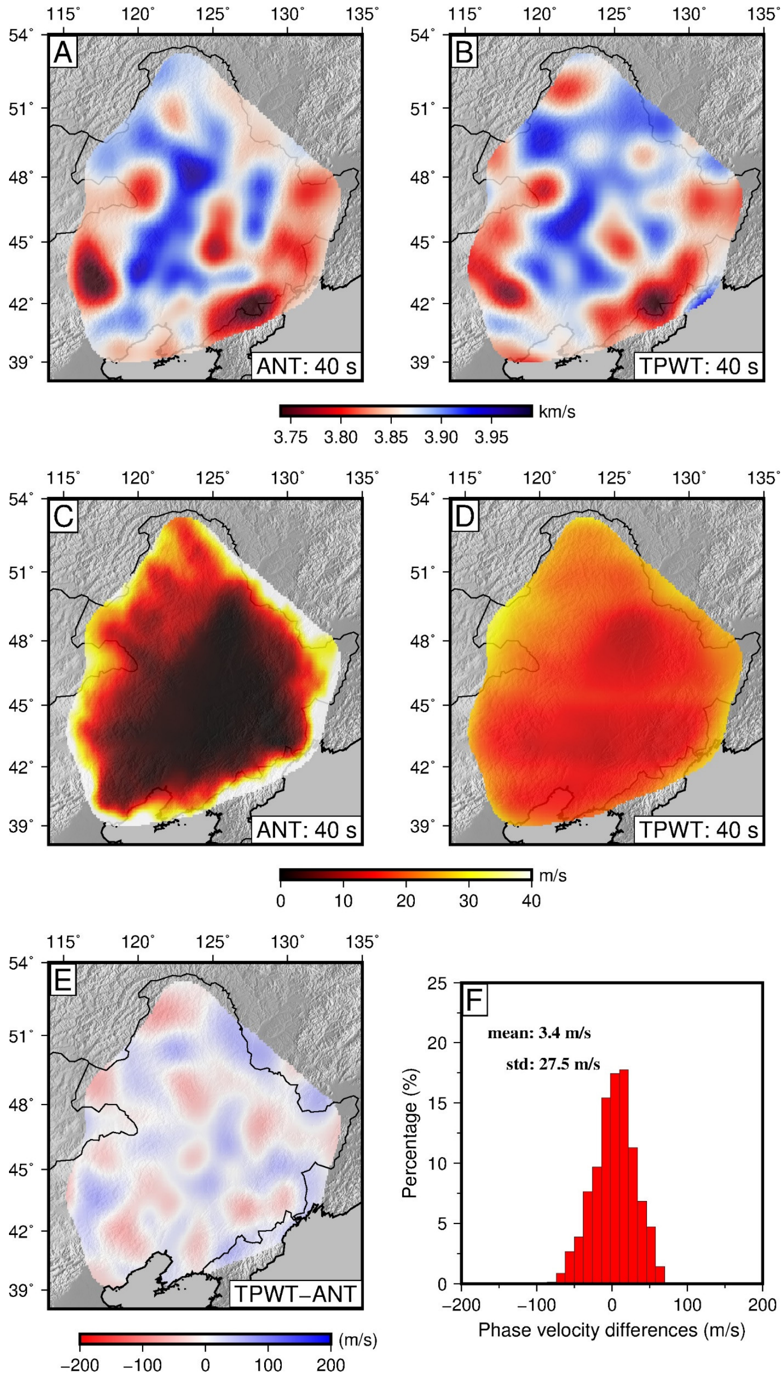

Figure S7. Comparison between the 40 s phase velocity maps derived from the ambient noise tomography (A) and earthquake two-plane wave tomography (B) with the corresponding uncertainty maps shown in (C) and (D). (E) The difference of phase velocity maps between the two methods (ambient noise tomography subtracted from earthquake two-plane wave tomography). (F) Histogram of phase velocity differences between the two methods. The mean difference and standard deviation of the difference are indicated inside the panel.

CHECKERBOARD RESOLUTION TEST

Conventional checkerboard tests are conducted to evaluate the resolution of our inverted phase velocity models (Fig. S8). The input model (Fig. S8A) consists of alternating positive and negative velocity anomalies of ±5% with a cell size of 1.5° × 1.5° (corresponding to anomaly with the spatial dimension of around 150 km × 150 km). The ray path distribution for the synthetic computation of phase velocities and regularization employed in the synthetic inversion are all kept the same as the real inversion. For the ambient noise tomography, the input model is largely recovered throughout the period band with some smearing effects observed at the edges of the study region owing to the relatively insufficient ray coverage (Figs. S8A-S8E). For the earthquake two-plane wave tomography, the input model is generally well recovered, although the magnitude of anomaly and model resolution degrade noticeably as period increases (Figs. S8F-S8I), which can be explained by the depreciated structural sensitivity of Rayleigh-waves at longer periods.

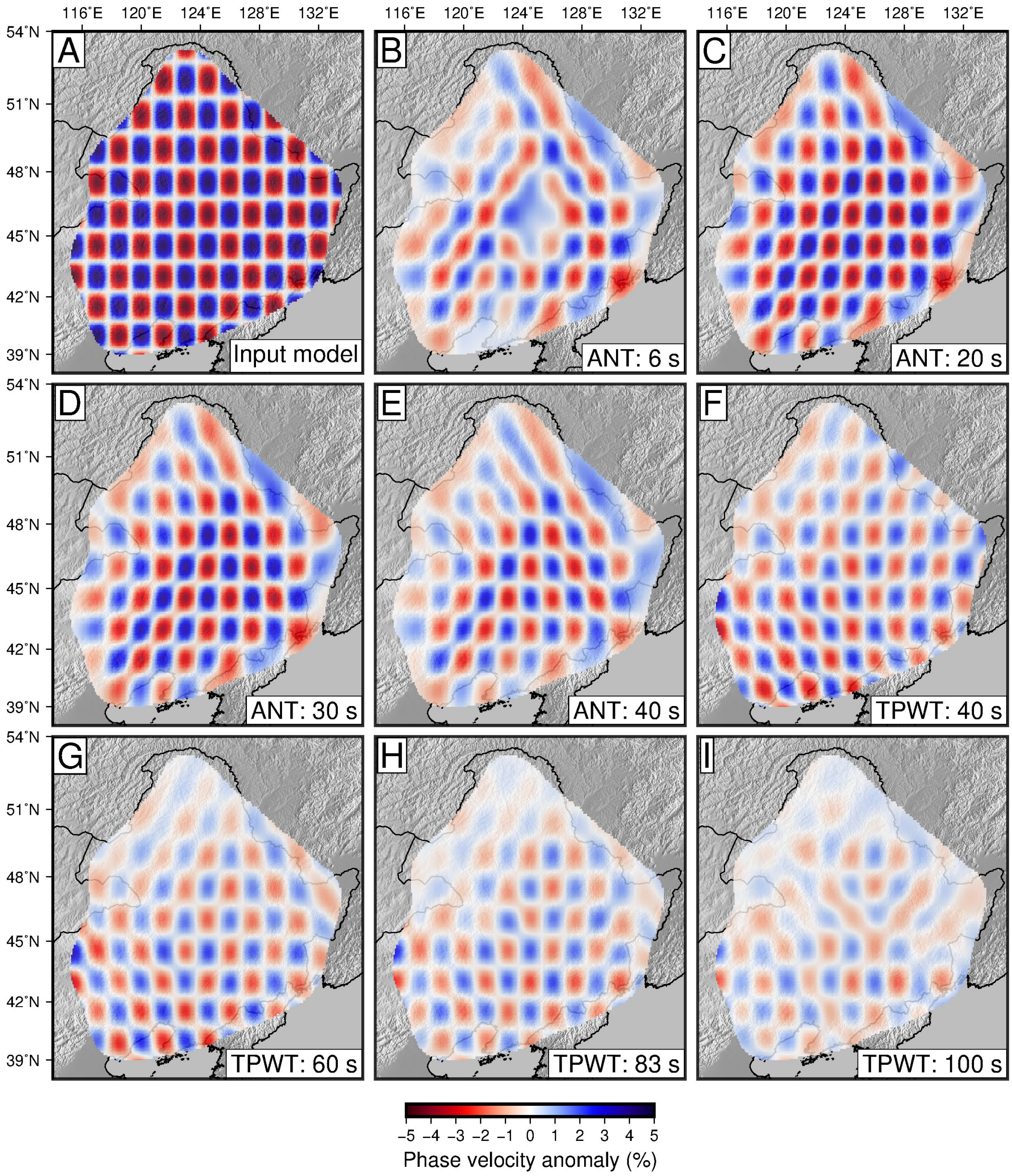

Figure S8. Checkerboard test for the ambient noise tomography (ANT) and earthquake two-plane wave tomography (TPWT). (A) Input model consisting of velocity anomalies of ±5% with a cell size of 1.5° × 1.5°. (B-E) Recovered models for the ambient noise tomography at different periods. (F-I) Recovered models for the earthquake two-plane wave tomography at different periods.

S-WAVE VELOCITY STRUCTURE INVERSION

Inversion approach and model parameterization

Local dispersion curve at each 0.5°×0.5° grid node is extracted by combining phase velocities derived from the ambient noise and earthquake two-plane wave tomography at the period band of 6-143 s. For periods shorter than 40 s and longer than 50 s, the corresponding phase velocities are purely taken from the ambient noise and earthquake two-plane wave tomography, respectively. At the overlapped period band of 40-50 s, we take a linearly weighted average of phase velocities from the two datasets. This means that as period increases from 40 to 50 s, the relative weights assigned to the ambient noise data and earthquake two-plane wave data linearly decrease from 1 to 0 and increase from 0 to 1, respectively. After performing two tests with only one or the other phase velocity chosen from the two datasets at the 40-50 s period band in the Vs inversion, we found that the two resultant Vs images are both nearly identical to the previous images (Figs. 2 and 3) without any noticeable differences. This implies that the weighting scheme invoked at the overlapped period band actually has little effect on the final Vs inversion results, since the phase velocity structures derived from the two methods are very similar to each other at overlapped periods (Figs. S7A and S7B) and the standard deviation of the difference between the two maps (Fig. S7F) is generally comparable to the standard deviation of each individual method (Figs. S7C and S7D).

1-D Vs profile beneath each individual node is obtained by inverting the extracted local dispersion curve with a Markov chain Monte Carlo inversion algorithm (Guo et al., 2016). The 1-D Vs structure is parameterized as a sedimentary layer, a crystalline crustal layer and a mantle layer down to 300-km depth with four and five B-spline coefficients employed to describe the velocity variations in the crystalline crust and upper mantle, respectively. The thicknesses of the sedimentary and crystalline crustal layers are set as unknowns and inverted simultaneously with the S-wave velocities. During the inversion, the priori searching range of S-wave velocity is set to be ±20% relative to the starting PREM model (Dziewonski and Anderson, 1981). The initial thickness of the sedimentary layer is retrieved from the CRUST1.0 model (Laske et al., 2013), and the Moho is allowed to vary ±3 km from the starting model constrained by a previous receiver function study of He et al. (2014). Crustal Vp/Vs ratio is also taken from He et al. (2014), and in the upper mantle, Vp/Vs ratio is set as a constant of 1.732. Then, the local 1-D Vp profile is scaled from the Vs structure based on the Vp/Vs ratio. Local 1-D density profile is related to Vp using the Birch's law (Birch, 1961). Physical dispersion correction is applied to our Vs model based on the attenuation (Q) values from the PREM model (Dziewonski and Anderson, 1981). One additional constraint is that the velocity jump across the Moho is required to be positive (i.e. mantle Vs > lower crustal Vs). For each grid node, the resulting 1-D Vs model is determined from the statistics of the posterior probability density function (PDF) using the last 3,000 accepted models in the Markov chain.

1-D and 3-D Vs models

Examples of three inverted 1-D Vs profiles and corresponding posterior PDFs at selected points located at the CBS, WDLC and SLB (green dots in Figure 2F) are plotted in Figures S9B, S9D and S9F, respectively. Predicted surface wave dispersion curves are shown as thin gray lines along with the observations represented by blue and red dots for the ambient noise and earthquake two-plane wave tomography, respectively (Figs S9A, S9C and S9E). For comparison, the inverted 1-D Vs profiles for the three selected grid nodes, and the regional averaged 1-D Vs profile are depicted in Figure S10. As illustrated in Figure S10, 1-D Vs profile beneath the CBS volcano shows significant low velocities both in the crust and upper mantle compared to the regional average, whereas 1-D Vs profile beneath the WDLC volcano is generally close to the regional average. The final 3-D Vs model of NE China is constructed by assembling all the 1-D Vs profiles in the study region. Vertical profiles (with the surface locations indicated in Figure 1A) of Vs perturbations calculated relative to the regional average (black line in Figure S10) is plotted in Figure S11. Horizontal slices and cross sections of absolute Vs are displayed in the main text as Figure 2 and Figure 3, respectively.

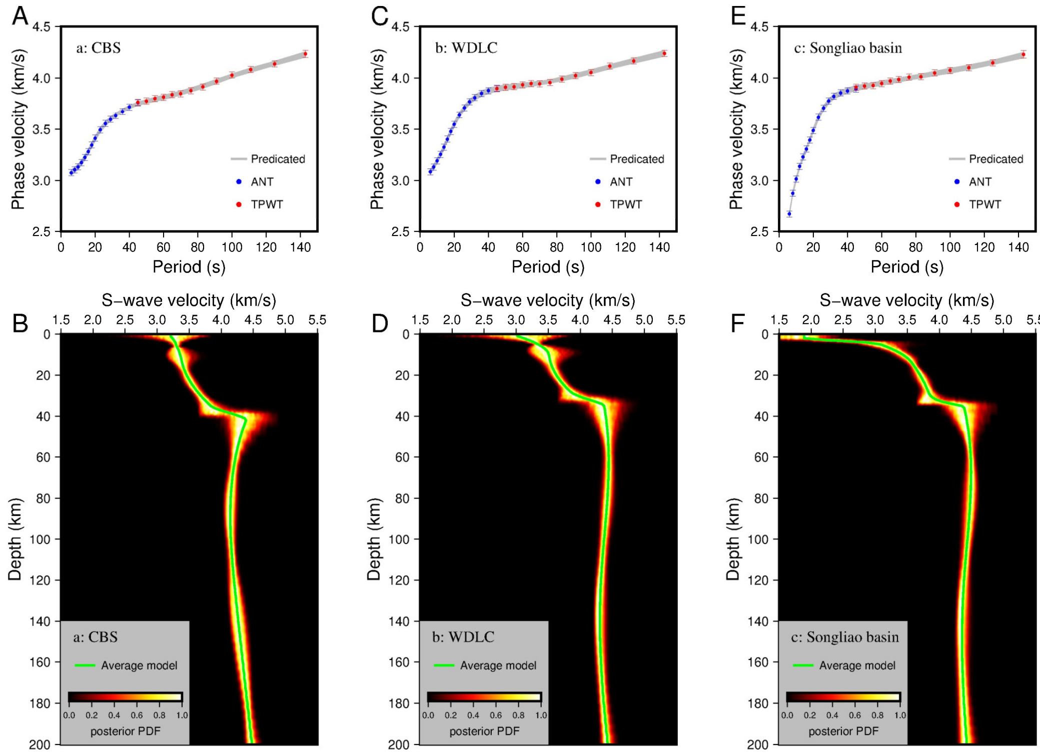

Figure S9. (A, C, E) The blue and red dots represent the observed Rayleigh-wave phase velocity dispersion data from the ambient noise and two-plane wave tomography, respectively, with their locations shown in Figure 2F (green stars). The thin gray lines display the predicted Rayleigh-wave phase velocity dispersion curves calculated from the 3,000 accepted models. (B, D, F) Ensembles of 1-D Vs models inverted from the observed Rayleigh-wave phase velocity dispersion data as shown in A, C and E, respectively. The color scale stands for the normalized posterior PDF, in which lighter color corresponds to higher probability distribution of the Vs. The thick green line represents the averaged model from the 3,000 best fit samples.

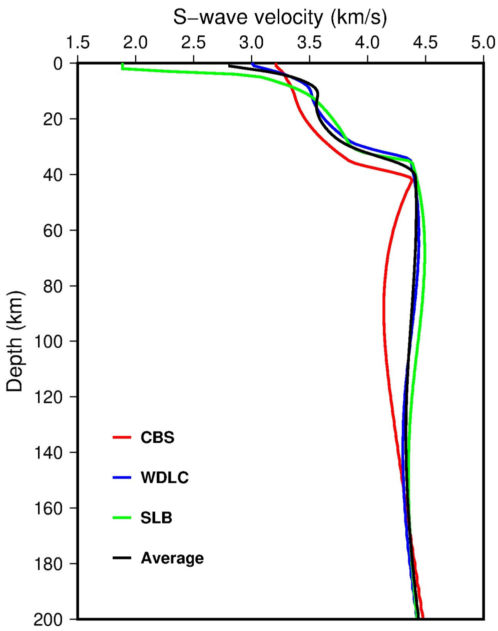

Figure S10. The red, blue and green lines represent the 1-D Vs profiles (also shown in Figures S9B, S9D and S9F) for the three grid nodes (marked as green stars in Figure 2F) located at the CBS, WDLC and SLB, respectively. The black line shows the regional average 1-D Vs profile.

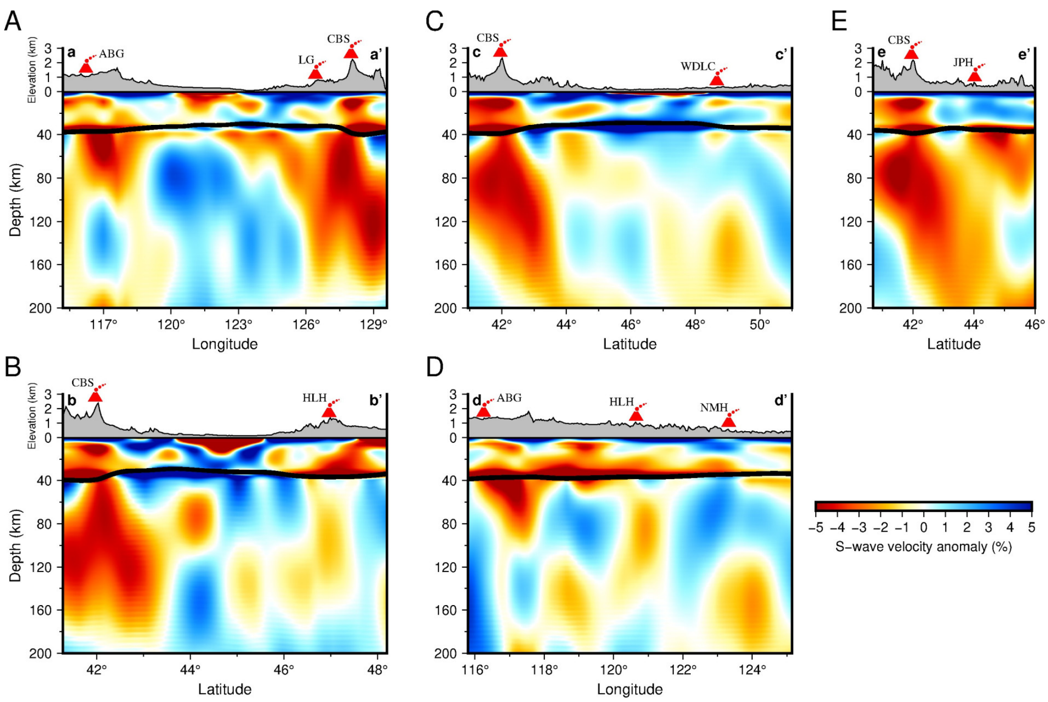

Figure S11. Cross-sectional view of S-wave velocity perturbations calculated relative to the regional average (black line in Figure S10) below the Quaternary intraplate volcanic fields in NE China. Corresponding profile locations are indicated by the purple solid lines in Figure 1A.

SYNTHETIC RESTORING TEST

To evaluate the reliability of our Vs inversion results, we conduct a synthetic restoring test to check whether we can robustly recover the primary imaging features interpreted in this study. The input model (Fig. S12A) is designed according to the imaged low/high Vs bodies shown in Figure 3C. The amplitude of input low/high Vs bodies are calculated relative to the regional average Vs at corresponding depths along the chosen profile. The upper and lower parts of the upper mantle low-velocity shapes beneath the CBS volcano are given a 6% and 5% Vs reduction, respectively. The high-velocity lid beneath the WDLC volcano and the small-scale low-velocity body atop are set with a 4% Vs increase and 4% Vs reduction, respectively. The bottom low-velocity shape beneath the WDLC volcano is given a 4% Vs reduction as well. The crustal region (above 40 km) is set with 1-D background Vs without perturbations.

We first generate synthetic phase velocity data based on the given input model and then perform the ambient noise tomography, earthquake two-plane wave tomography, and Vs inversion consecutively using the same ray path and inversion parameters as those applied to the real data. The output model (Fig. S12B) demonstrates that the input upper mantle velocity anomalies beneath the CBS and WDLC volcanoes, including the localized low-velocity body atop the high-velocity lid beneath the WDLC volcano, can all be adequately recovered, indicating that the main features we interpret in this study are well resolved, though some horizontal and vertical smearing effects occur surrounding the input velocity anomalies. The output model (Fig. S12B) shows that the input low-velocity anomalies in the uppermost mantle beneath the CBS and WDLC volcanoes appear to “leak” into the lower crust a little bit due to vertical smearing effects. Nevertheless, the background crustal structure is generally well recovered, especially for regions without underlying upper mantle velocity anomalies (Fig. S12).

It has been well documented that surface waves are mostly sensitive to lateral variations of Vs structures. As a result, vertical (depth) resolution in surface wave tomography is relatively lower compared to horizontal resolution, especially when it comes to layered anomalies with alternating positive and negative perturbations, which is the case of our synthetic restoring test as shown in Figure S12. On the other hand, however, we can see that the recovered high-velocity body (Fig. S12B) does reflect the model feature, though being visibly smeared in pattern and underestimated in amplitude compared to the input velocity anomaly (Fig. S12A). This therefore suggests that the high-velocity lid imaged beneath the WDLC is a rather robust feature, and that it may be even more prominent in reality than in the inversion result.

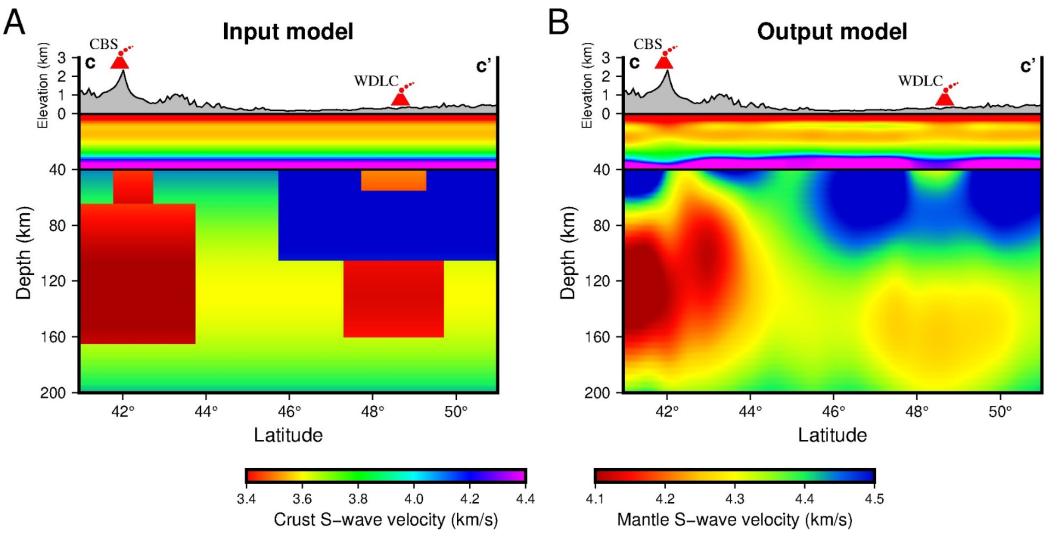

Figure S12. Synthetic restoring test. (A) Cross-section of the input model resembling the cc' profile as depicted in Figure 3C. The amplitude of input low/high Vs bodies are calculated relative to the regional average Vs (black line in Figure S10) at corresponding depths. (B) Cross-section of the output model, which is obtained by generating synthetic phase velocity data from the input model (A) and then performing the ambient noise tomography, two-plane wave tomography, and Vs inversion consecutively using the same ray path and inversion parameters as applied to the real data.

REFERENCES

Barmin, M.P., Ritzwoller, M.H., and Levshin, A.L., 2001, A fast and reliable method for surface wave tomography: Pure and Applied Geophysics, v. 158, p. 1351-1375, https://doi.org/10.1007/PL00001225.

Bensen, G.D., Ritzwoller, M.H., Barmin, M.P., Levshin, A.L., Lin, F., Moschetti, M.P., Shapiro, N.M., and Yang, Y., 2007, Processing seismic ambient noise data to obtain reliable broad-band surface wave dispersion measurements: Geophysical Journal International, v. 169, p. 1239-1260, https://doi.org/10.1111/j.1365-246X.2007.03374.x.

Birch, F., 1961, The velocity of compressional waves in rocks to 10 kilobars: 2.: Journal of Geophysical Research, v. 65, p. 2199-2224, https://doi.org/10.1029/JZ066i007p02199.

Dziewonski, A.M., and Anderson, D.L., 1981, Preliminary reference Earth model: Physics of the Earth and Planetary Interiors, v. 25, p. 297-356, https://doi.org/10.1016/0031-9201(81)90046-7.

Forsyth, D.W., and Li, A., 2005, Small-scale convection and anisotropy in the mantle beneath southern California from high-resolution Rayleigh wave tomography: Seismic Earth: Array Analysis of Broadband Seismograms, v. 157, p. 81-97, https://doi.org/10.1029/157GM06.

Guo, Z., Chen, Y.J., Ning, J.Y., Yang, Y.J., Afonso, J.C., and Tang, Y.C., 2016, Seismic evidence of on-going sublithosphere upper mantle convection for intra-plate volcanism in Northeast China: Earth and Planetary Science Letters, v. 433, p. 31-43, https://doi.org/10.1016/j.epsl.2015.09.035.

He, R.Z., Shang, X.F., Yu, C.Q., Zhang, H.J., and Van der Hilst, R.D., 2014, A unified map of Moho depth and Vp/Vs ratio of continental China by receiver function analysis: Geophysical Journal International, v. 199, p. 1910-1918, https://doi.org/10.1093/gji/ggu365.

Laske, G., Masters, G., Ma, Z.T., and Pasyanos, M., 2013, Update on CRUST1.0—A 1-degree global model of Earth's crust: Geophysical Research Abstract, v. 15, p. Abstract EGU2013-2658.

Levshin, A.L., and Ritzwoller, M.H., 2001, Automated detection, extraction, and measurement of regional surface waves: Pure and Applied Geophysics, v. 158, p. 1531-1545, https://doi.org/10.1007/PL00001233.

Lu, M.W., Lei, J.S., Zhao, D.P., Ai, Y.S., Xu, X.W., and Zhang, G.B., 2020, SKS splitting measurements in NE China: New insights into the Wudalianchi intraplate volcanism and mantle dynamics: Journal of Geophysical Research: Solid Earth, v. 125, p. e2019JB018575, https://doi.org/10.1029/2019JB018575.

Peng, Y.B., Jiang, M.M., Ai, Y.S., 2019. Efficient scheme to extract Green functions of Rayleigh wave from seismic noise via a Python library for seismology-ObsPy (In Chinese with English abstract): Progress in Geophysics , v. 34, p. 919-927, https://doi.org/10.6038/pg2019CC0119.

Ri, K.S., Hammond, J.O.S., Ko, C.N., Kim, H., Yun, Y.G., Pak, G.J., Ri, C.S., Oppenheimer, C., Liu, K.W., Iacovino, K., and Ryu, K.R., 2016, Evidence for partial melt in the crust beneath Mt. Paektu (Changbaishan), Democratic People's Republic of Korea and China: Science Advances, v. 2, https://doi.org/10.1126/sciadv.1501513.

Tao, K., Niu, F.L., Ning, J.Y., Chen, Y.S.J., Grand, S., Kawakatsu, H., Tanaka, S., Obayashi, M., and Ni, J., 2014, Crustal structure beneath NE China imaged by NECESSArray receiver function data: Earth and Planetary Science Letters, v. 398, p. 48-57, https://doi.org/10.1016/j.epsl.2014.04.043.

Wang, X., Chen, Q.F., Li, J., and Wei, S.J., 2016, Seismic sensor misorientation measurement using P-wave particle motion: An application to the NECsaids Array: Seismological Research Letters, v. 87, p. 901-911, https://doi.org/10.1785/0220160005.

Yang, Y.J., and Forsyth, D.W., 2006, Regional tomographic inversion of the amplitude and phase of Rayleigh waves with 2-D sensitivity kernels: Geophysical Journal International, v. 166, p. 1148-1160, https://doi.org/10.1111/j.1365-246X.2006.02972.x.

Zhang, F.X., and Wu, Q.J., 2019, Velocity structure in upper mantle and its implications for the volcanism nearby the north edge of Songliao Basin (In chinese with English abstract): Chinese Journal of Geophysics, v. 62, p. 2918-2929, https://doi.org/10.6038/cjg2019M0665.

Zhang, K.W., Chen, Q.F., and Chen, Y., 2020, Crustal structure beneath the southwestern Xing'an-Mongolia Orogenic Belt revealed by receiver function analysis (In Chinese with English abstract): Chinese Journal of Geophysics, v. 63, p. 1484-1504, https://doi.org/10.6038/cjg2020N0048.

Zheng, X.F., Yao, Z.X., Liang, J.H., and Zheng, J., 2010, The role played and opportunities provided by IGP DMC of China National Seismic Network in Wenchuan earthquake disaster relief and researches: Bulletin of the Seismological Society of America, v. 100, p. 2866-2872, https://doi.org/10.1785/0120090257.

Zhou, Y., Dahlen, F.A., and Nolet, G., 2004, Three-dimensional sensitivity kernels for surface wave observables: Geophysical Journal International, v. 158, p. 142-168, https://doi.org/10.1111/j.1365-246X.2004.02324.x.